Journal of Geophysical Research: Oceans

RESEARCH ARTICLE
10.1029/2017JC013664

Ice Shelf Rift Propagation and the Mechanics of Wave-Induced Fracture

Bradley Paul Lipovsky[1]

[1]Department of Earth and Planetary Sciences, Harvard University, Cambridge, MA, USA

Key Points:
- I infer ice shelf wave-induced stresses and then relate these stresses to a rift propagation criterion based in inertial fracture mechanics
- The lack of rift propagation during periods of high wave-induced stresses suggests the existence of additional rift strengthening
- Ice shelf rifts may be stabilized as they propagate into deeper water or thinner ice

Correspondence to:
B. P. Lipovsky,
brad_lipovsky@fas.harvard.edu

Citation:
Lipovsky, B. P. (2018). Ice shelf rift propagation and the mechanics of wave-induced fracture. *Journal of Geophysical Research: Oceans*, *123*. https://doi.org/10.1029/2017JC013664

Received 28 NOV 2017
Accepted 28 APR 2018
Accepted article online 5 MAY 2018

Abstract Distant storms, tsunamis, and earthquakes generate waves on floating ice shelves. Previous studies, however, have disagreed about whether the resulting wave-induced stresses may cause ice shelf rift propagation. Most ice shelf rifts show long periods of dormancy suggesting that they have low background stress concentrations and may therefore be susceptible to wave-induced stresses. Here I quantify wave-induced stresses on the Ross Ice Shelf Nascent Rift and the Amery Ice Shelf Loose Tooth T2 Rift using passive seismology. I then relate these stresses to a fracture mechanical model of rift propagation that accounts for rift cohesive strength due to refrozen melange, ice inertia, and spatial heterogeneity in fracture toughness due to the presence of high toughness suture zones. I infer wave-induced stresses using the wave impedance tensor, a rank three tensor that relates seismically observable particle velocities to components of the stress tensor. I find that wave-induced stresses are an order of magnitude larger on the Ross Ice Shelf as compared to the Amery Ice Shelf. In the absence of additional rift strength, my model predicts that the Nascent Rift should have experienced extensive rift propagation. The observation that no such propagation occurred during this time therefore suggests that the Nascent Rift experiences strengthening from either refrozen melange or rift tip processes zone dynamics. This study illustrates one way in which passive seismology may illuminate glacier calving physics.

1. Introduction

Floating ice shelves exert a net buttressing force on grounded ice and therefore support the stability of ice sheets (Doake et al., 1998; Rignot et al., 2004; Scambos et al., 2004). The extent of ice shelfs is often limited by the formation of 10–100 km long, through-thickness fractures called rifts. Rifts tend to grow in length until they connect to the ice front and create a tabular iceberg (Jacobs et al., 1986; Keys et al., 1998; Robin, 1979; Shabtaie & Bentley, 1982). Observations show that rifts experience most of their growth during episodic bursts of activity (Joughin & MacAyeal, 2005) that last from seconds (Banwell et al., 2017; Powell, 2015) to hours (Bassis et al., 2005). These short time scales suggest that rift propagation is a brittle process, meaning that during episodes of rift propagation the ice shelf is well approximated as an elastic solid everywhere except in a small region near the rift tip (Broek, 2012). Ductile fracture, in contrast, may occur by the slow coalescence of microcracks (Borstad et al., 2012, 2013; Duddu et al., 2013; Duddu & Waisman, 2013; Lemaitre, 1985; Pralong & Funk, 2005; Rice & Tracey, 1969; Weiss, 2004) and results in an essentially viscous-plastic ice rheology. Field observations show that ductile fracture also occurs in ice shelf rifts, although it typically is associated with slower growth (Bassis et al., 2007). Linear elastic fracture mechanics is well suited to describe brittle fracture and has previously been used in the study of ice shelf rift propagation, crevasse growth, calving, and hydrofracture (Alley et al., 2005; Krawczynski et al., 2009; Krug et al., 2014; Larour et al., 2004a; Nemat-Nasser et al., 1979; Plate et al., 2012; Rist et al., 2002; Scambos et al., 2009a; Smith, 1976; Van der Veen, 1998; Yu et al., 2017; Weertman, 1971, 1973).

Brittle fracture is driven by loading applied to sharp geometrical features such as the tip of an ice shelf rift (Griffith, 1921). The resulting stress concentration may be quantified using the stress intensity factor K (Irwin, 1957). The stress intensity factor K may in turn be expressed entirely in terms of the loading exerted on a system (Rice, 1968), which in ice shelves consists of contributions from gravity, buoyancy, and interaction with grounded and floating ice (Reeh, 1968; Weertman, 1957). Catalogs of Antarctic ice shelf rifts, however, show that this loading often results in zero measurable propagation over years to decades of observation (Walker et al., 2013, 2015). Rift propagation, when it does occur, is typically observed to be highly episodic

in time (Bassis et al., 2005). In the context of linear elastic fracture mechanics, this observation suggests that ice shelf rifts commonly attain a state of stress such that $K < K_c$ and no propagation occurs. I argue that this is the precise setting that allows ocean waves to effectively drive episodic ice shelf rift propagation.

The exact mechanism responsible for the episodic nature of ice shelf rift propagation remains the subject of multiple competing hypotheses in the literature. Three processes have been proposed as being of importance: spatial heterogeneity of fracture toughness, constitutive instability, and temporal variation in loading due to interaction with ocean waves. In regards to spatial heterogeneity, ice shelf suture zones that form at provenance boundaries in the ice shelf appear to be particularly important. Rapid rift tip propagation events are often observed to terminate when the rift tip reaches an ice shelf suture zone (Borstad et al., 2017; Hulbe et al., 2010; McGrath et al., 2014). Wave action also appears to play a role. In studies of the Nascent Rift, MacAyeal et al. (2006) and Cathles et al. (2009) revived the idea of Holdsworth and Glynn (1978) that wave-induced stresses might cause rift propagation. However, Bassis et al. (2005, 2007, 2008) also analyzed in situ seismic data from the Loose Tooth and concluded that rift propagation there was driven primarily by glacial stresses. Although other studies have appeared to confirm the importance of wave action in rift propagation, these studies were limited by not having in situ seismic data. Using remotely sensed imagery, Brunt et al. (2011) observed rift propagation following the arrival of a tsunami. Banwell et al. (2017) used a nearby seismometer located on bedrock to show that a rift propagation event on the McMurdo Ice Shelf occurred during the arrival of large amplitude ocean waves from a distant storm. Finally, a constitutive instability, essentially the opening-mode equivalent of the shearing-mode stick-slip instability (Lipovsky & Dunham, 2016, 2017), has been proposed to be important for episodic rift motion (Larour et al., 2004a). One of the goals of this paper is to develop a theoretical framework within which to compare the predictions of these hypotheses.

Seismometers located directly on floating ice shelves quantify the ice shelf wave field. Using an appropriately defined transfer function called the wave impedance it is therefore possible to calculate stresses from in situ velocity seismograms. In a similar vein, Williams and Robinson (1981) used a transfer function approach to estimate water pressure fluctuations from 1 min period gravimeter measurements on the Ross Ice Shelf. The stresses carried by waves in ice shelves have been previously analyzed in an idealized geometry by Holdsworth and Glynn (1978) and Sergienko (2010, 2013) and in more realistic geometries by Konovalov (2014) and Sergienko (2017). Each of these studies, however, calculated the ice shelf response to idealized, monochromatic wave forcing. Here I build on these previous studies by estimating the stresses associated with the in situ ice shelf wave fields as recorded by seismometers located on floating ice shelves. I begin this paper in the first section by describing ice shelf wave impedances (section 2).

I describe a fracture mechanical model of ice shelf rift propagation in section 3. I then apply this model to the wave-induced stresses inferred at sites near the Ross Ice Shelf Nascent Rift and the Amery Ice Shelf Loose Tooth Rift (sections 4 and 5). These ice shelves are shown in Figure 1. The principal finding of this analysis is that, in the absence of some additional source of rift strength, wave-induced stresses are predicted to have been sufficiently large to cause rift propagation on the Nascent Rift. Satellite imagery, however, shows that no observable rift propagation occurred during the observation periods under consideration. This finding therefore suggests that the Nascent Rift experienced strengthening that prevented rift propagation during this time. One potential source of this strength is refreezing in the rift-filling melange (Fricker et al., 2005; Larour et al., 2004b; MacAyeal et al., 1998; Rignot & MacAyeal, 1998). This and other topics are discussed in section 6.

The analysis presented here connects qualitative predictions of ice shelf instability (Holdsworth & Glynn, 1978) to geophysical measurement (Bassis et al., 2007; Bromirski et al., 2017; Brunt et al., 2011; Cathles et al., 2009; MacAyeal et al., 2006) and therefore unleashes the power of seismology to elucidate the detailed mechanics of ice shelf rift propagation.

2. Wave Stresses

Seismometers located directly on floating ice shelves measure the Lagrangian particle velocity, within a certain frequency range, of the parcel of ice on which they rest. In this section, I derive a transfer function called the wave impedance that relates these particle velocity perturbations to their associated stresses perturbations. I calculate wave impedances for two types of long period ice shelf waves: flexural waves and extensional waves. I will show that there are two main differences between these wave types. First, the

flexural wave impedance is frequency-dependent but the extensional wave impedance is not. Second, flexural wave impedances tend to be much higher than extensional wave impedances. These results are summarized in Figures 2 and 3.

In order to write down expressions for the wave impedances, it is first necessary to describe the waves themselves. In Appendix A, I describe ice shelf wave motion in a finite-thickness elastic ice shelf over an inviscid, incompressible, finite-thickness water layer and rigid ocean floor. I consider waves that propagate in the direction of flow, and I treat a two-dimensional cross section in the vertical and flow directions. Several limitations associated with these assumptions are discussed in section 6. In Appendix B I show that waves with wavelength greater than the ice thickness may propagate as either flexural or extensional waves. I begin this section by describing the general wave impedance transfer function (section 2.1).

2.1. Ice Shelf Wave Impedances

The transfer function between the perturbation velocity vector component $v_l \equiv \partial u_l/\partial t$ and the perturbation stress tensor component σ_{ij} is called the wave impedance. It is defined as:

$$Z_{ijl}(k,\omega)=\frac{\Sigma_{ij}(k,\omega)}{(-i\omega)U_l(k,\omega)}. \tag{1}$$

Here the subscripts i, j, and l may vary over the three spatial coordinates x, y, and z. The spatial coordinates are defined so that x is in the direction of ice flow, z is positive upward, and y is perpendicular to x and z following the right-hand rule. Upper case letters denote the double Fourier transform in time t and in the horizontal direction x. For an arbitrary, adequately smooth function f, the Fourier transform of f is denoted,

$$F(k,z,\omega)=\int_{-\infty}^{\infty}\int_{-\infty}^{\infty} f(x,z,t)e^{i(kx-\omega t)}\mathrm{d}x\mathrm{d}t \tag{2}$$

This definition introduces the horizontal wave number k and frequency ω.

The impedance tensor defined in this way allows the estimation of wave field stresses using multiplication in the Fourier domain,

$$\sigma_{ij}(x,t)=\int_{-\infty}^{\infty}\int_{-\infty}^{\infty} Z_{ijl}(k,\omega)U_l(k,\omega)e^{i(kx-\omega t)}\mathrm{d}k\mathrm{d}\omega. \tag{3}$$

The exact form of the wave impedance tensor components depends on the type of wave being considered. For both flexural and extensional waves, the wave impedance is a function of the wave phase velocity. These wave phase velocities are derived in Appendix B, and the associated particle motions are described in Appendix C.

2.2. Flexural Waves

The impedance of a wave generally depends on the wave phase velocity $c \equiv \omega/k$. Writing in terms of the wavelength $\lambda \equiv 2\pi/k$, the phase velocity of flexural-gravity waves is determined by the dispersion relation:

$$\omega^2=\frac{2\pi g}{\lambda}\frac{\left(\lambda_{fg}/\lambda\right)^4+1}{2\pi(\rho/\rho_w)h/\lambda+\coth\left(2\pi H/\lambda\right)}, \tag{4}$$

with water layer thickness H, ice thickness h, acceleration due to gravity g, flexural-gravity wave length λ_{fg},

$$\lambda_{fg} \equiv 2\pi\left(\frac{D}{g\rho_w}\right)^{1/4}, \tag{5}$$

flexural rigidity $D \equiv E'h^3$, $E' \equiv E/(1-\nu^2)$, Young's Modulus E, and Poisson ratio ν. The material properties of ice are listed in Table 1. At the tip of the Nascent and Loose Tooth Rifts, λ_{fg}=7.1 and 7.8 km, respectively (Fretwell et al., 2013).

The flexural-gravity wave length λ_{fg} separates two regimes of wave behavior (Figure 2). When $\lambda \gg \lambda_{fg}$ the dispersion relation is identical to that for surface gravity waves. In contrast, when $\lambda \ll \lambda_{fg}$, the dominant restoring force is elasticity and gravity does not enter the

Table 1
Table of Ice Mechanical Properties (Schulson et al., 2009)

Shear modulus	μ	3.5 GPa
Young's modulus	E	9.3 GPa
Poisson ratio	ν	0.33
Density of ice	ρ	916 kg/m^3
Density of seawater	ρ_w	1,024 kg/m^3
Dilatational wave speed	c_p	3,750 m/s
Shear wave speed	c_s	1,950 m/s
Fracture toughness	K_c	100–400 kPa$\sqrt{\text{m}}$

dispersion relation. As described in detail in Appendix B, this dispersion relation is valid for waves with wavelength greater than the ice thickness.

I calculate the flexural mode σ_{xx}-to-u_z impedance component as:

$$Z^F_{xxz} = \frac{\Sigma_{xx}}{(-i\omega)U_z} \approx (-i\omega)\frac{hE'}{[c(\omega)]^2}. \tag{6}$$

In writing equation (6), I have used the expressions for the extensional wave stress Σ_{xx} and vertical displacement U_z derived in Appendix C. The approximate equality symbol reflects the long wavelength approximation as discussed in Appendix B.

This impedance component is plotted in Figure 2. Flexural wave impedance reaches a maximum at the frequency associated with the flexural-gravity wavelength λ_{fg}. Below this frequency, impedance increases proportional to frequency ω. Above this frequency, impedance is a decreasing function of frequency.

Flexural stresses, denoted σ_f, may be calculated from a vertical component velocity seismogram $v_z(t) = \partial u_z/\partial t$ by convolving a velocity time series with the transfer function in equation (6),

$$\sigma_f(t) \equiv \sigma_{xx}(t) = E'h\int \frac{(-i\omega)V_z(\omega)}{[c(\omega)]^2} e^{i\omega t}\, \mathrm{d}\omega. \tag{7}$$

In this expression, I have used the definition of the phase velocity to eliminate reference to the wave number k.

A simplified case occurs for wavelengths longer than the water depth H and the flexural-buoyancy wavelength λ_{fg}. In this case $c^2 = gH$ is nondispersive and therefore independent of frequency. The integral in equation (7) may therefore be evaluated as:

$$\sigma_f(t) = \frac{E'h}{gH}\frac{\partial V}{\partial t}. \tag{8}$$

This result is interesting because it shows that waves in the gravity limit have stresses that are proportional to particle acceleration. This is in contrast to body waves which have stresses that are proportional to particle velocity.

2.3. Extensional Waves

Extensional waves have nondispersive phase velocity

$$\frac{\omega}{k} = \sqrt{\frac{E'}{\rho}}. \tag{9}$$

This phase velocity is the plane strain equivalent of the wave speed in a one-dimensional elastic bar, $\sqrt{E/\rho}$. For the material properties of ice (Table 1), this phase velocity is equal to 3,375 m/s. The extensional mode does not exhibit any ice-ocean interaction (Appendix A). As was also the case for flexural-gravity waves, this dispersion relation is only valid for waves with wavelength greater than the ice thickness (Appendix B).

The extensional mode has σ_{xx}-to-u_x impedance component,

$$Z^E_{xxx} = \frac{\Sigma_{xx}}{(-i\omega)U_x} \approx -\sqrt{\frac{2\rho\mu}{1+\nu}}. \tag{10}$$

For the material properties of ice $Z^E_{xxx} \approx 2.07$ kPa/(mm/s). This value differs from the corresponding S wave impedance by a factor of $\sqrt{2/(1+\nu)} \approx 1.23$.

Extensional stresses, denoted σ_e, may be calculated from a horizontal component velocity seismogram $v_x(t) = \partial u_z/\partial t$ as a simple time domain multiplication,

$$\sigma_e(t) \equiv \sigma_{xx}(t) = Z^E_{xxx} v_x(t). \tag{11}$$

3. Fracture Mechanics

I analyze brittle fracture using the energy-based Griffith fracture criterion (Griffith, 1921) expressed in terms of the stress concentration at the rift tip (Irwin, 1957). In this description, a preexisting fracture will grow in

length when its associated stress intensity factor K exceeds a critical value K_c called fracture toughness, a material property. For ice, K_c ranges between 150 and 400 kPa$\sqrt{\text{m}}$ (Rist et al., 2002). In section 6.4, I discuss the uncertainties associated with fracture toughness values.

The model developed in this section depicts the scenario where an ice shelf rift is loaded by wave-induced ocean stresses that are fast enough to be elastic but slow enough that inertia is negligible. As stresses increase over a wave period of tens to hundreds of seconds, the stress concentration at the rift tip increases. Once $K > K_c$, rift tip propagation occurs. In contrast to the loading stage, rift tip propagation may occur sufficiently rapidly so that the rate of propagation becomes limited by the inertia of the ice. Before proceeding with this treatment in section 3.1, I make two technical notes.

First, I note that inertia is negligible for perturbations with phase velocities far below the elastic waves speeds (see Appendix A). Such perturbations are called quasi-static to reflect that they are time dependent but have negligible inertial influence. In Appendix B, I demonstrate that the quasi-static approximation is valid for ice shelf flexural waves but not for extensional waves because long period extensional waves are not quasi-static. Treating the initiation of propagation as quasi-static is nonetheless a reasonable approximation for the data considered in this paper, however, because in section 5, I show that flexural stresses are much larger than extensional stresses and therefore are more likely to be responsible for the onset of rift propagation.

Second, I note that the applicability of linear elastic fracture mechanics rests on the condition of small scale yielding. Before continuing I verify this condition. Small scale yield occurs when all dimensions of a fractured object are much greater than the dimension of the plastic region surrounding the rift tip. An estimate of the plastic region size for an ideally elastic-plastic material is (Broek, 2012) $(K_c/\sigma_y)^2$, where $K_c \approx 100$ kPa m$^{1/2}$ is the fracture toughness of ice (Rist et al., 2002) and $\sigma_y \approx 100$ kPa is the yield stress of ice (Van der Veen, 1998). These estimates give a critical flaw size of about 1 m. Using a larger fracture toughness of $K_c \approx 400$ kPa m$^{1/2}$ gives plastic zone size 16 m. For typical ice shelf thicknesses of one to several hundred meters, we may safely proceed with a plane strain fracture mechanics treatment.

3.1. The Onset of Propagation

For a fixed geometry, the stress intensity factor is a linear functional of the stress tensor. The combined effects of background glacial loading and waves may therefore be treated by superposition,

$$K = K_{\text{glacial stresses}} + K_{\text{waves}}. \tag{12}$$

I treat the situation where the rift stress intensity factor K due to glacier stresses is lower than the fracture toughness $K < K_c$. This is a reasonable assumption for rifts which are dormant because under linear elastic fracture mechanics, a crack is expected to have zero propagation if and only if the stress intensity factor is below the fracture toughness $K < K_c$. The catalog of rifts published by Walker et al. (2013) shows that the majority of Antarctic rifts are dormant, thus suggesting that the analysis developed here applies to the majority of Antarctic rifts. For simplicity, I assume that $K_{\text{glacial stresses}} \approx 0$. Rift propagation would occur at a lower stress than predicted if $K_{\text{glacial stresses}} > 0$.

The stress intensity factor due to wave motion may then be broken into flexural and extensional components,

$$K \approx K_{\text{extension}} + K_{\text{flexure}}. \tag{13}$$

The stress intensity factor due to extensional motion is (Broek, 2012),

$$K_{\text{extension}} = \sigma_e \sqrt{\pi L/2}. \tag{14}$$

The stress intensity factor due to bending of a buoyantly floating plate is (Bažant, 1992),

$$K_{\text{flexure}} = |\sigma_f| \sqrt{\pi \lambda_{fg}}, \tag{15}$$

where the flexural-gravity wavelength is defined in equation (5). This stress intensity factor for bending of a floating plate is valid for rifts that are longer than the flexural-gravity wavelength.

3.2. Inertial Effects during Rift Tip Propagation

The rapid propagation of fractures requires accounting for elastoynamic effects. Freund (1972a, 1972b) was the first to generalize the analysis of Irwin (1957) to the elastodynamic case. He found that the stress intensity factor may be written as the product of static and dynamic terms,

$$K(L,\dot{L}) = \kappa(\dot{L}) K_0(L), \tag{16}$$

where an overdot denotes a time derivative. Here $K_0(L)$ is the time-independent stress intensity factor, which is identical to the stress intensity factor that would occur due to loading of a rift with instantaneous length L. The function κ has its origin in a particular elastodynamic transfer function, and is well approximated by

$$k(\dot{L}) \approx 1 - \frac{1}{c_r}\frac{\partial L}{\partial t}, \tag{17}$$

where c_r is the Rayleigh wave speed in ice. The conditions under which equation (16) is valid are quite general (Freund, 1998; Rice, 2001). Specifically, the existence of the factorization of the stress intensity factor into static and dynamic parts is independent of geometric and loading configuration.

Combining Equations (16) and (17) gives the rift tip equation of motion

$$\frac{\partial L}{\partial t} = \begin{cases} c_r \left[1 - \left(\frac{K_c}{K}\right)^2\right] & K \geq K_c \\ 0 & K < K_c \end{cases}. \tag{18}$$

This result has general features which have been noted previously (Freund, 1998), but are worth highlighting. In particular, the crack tip velocity has an instantaneous dependence on the stress level through the stress intensity factor K. This instantaneous response results because there is no sensitivity to the second derivative of L in equation (18). Integrating the rift tip velocity gives the rift propagation distance,

$$\delta L(t) = c_r \int_0^t \left\{1 - \frac{K_c[L(t')]}{K[\sigma(t'), L(t')]}\right\} \mathrm{d}t'. \tag{19}$$

I note that this description accounts for spatial variability in fracture toughness due, for example, to the presence of high toughness suture zones with accreted basal marine ice (Holland et al., 2009; Jansen et al., 2013; LeDoux et al., 2017; McGrath et al., 2012).

4. Observations of the Loose Tooth and Nascent Rifts

4.1. Rift Propagation Behavior

In this paper, I analyze two rifts, the Nascent Iceberg Rift on the Ross Ice Shelf and the Loose Tooth T2 Rift on the Amery Ice Shelf. I focus on observation periods during which seismic data is available: November 2005 to May 2006 on the Ross Ice Shelf and January to February 2007 on the Amery Ice Shelf. During these times, the Loose Tooth and Nascent Rifts were 17 and 46 km long (Scambos et al., 2007). The tip of the Nascent Rift was located in ice with thickness $h = 265$ m. The ocean floor was 691 m below sea level and the subshelf cavity was therefore $H = 479$ m thick. The tip of the Loose Tooth Rift was located in ice with thickness $h = 301$ m. The ocean floor was 734 m below sea level and the subshelf cavity was therefore $H = 466$ m thick. These geometries are compared in Figure 1.

During these time periods, neither rift exhibited measurable rift propagation. This is probably due to the fact that both rifts have propagated into ice suture zones that apparently have higher fracture toughness than the surrounding ice shelf (Borstad et al., 2017). I reach these conclusions by examining satellite imagery as archived in the Antarctic Ice Shelf Image Archive at the National Snow and Ice Data Center (Scambos et al., 2009b). These images are captured using the Moderate Resolution Imaging Spectroradiometer (MODIS) instrument. The observation that the Amery did not exhibit propagation during this time has been previously noted by Walker et al. (2015). The nominal resolution of 250 m places an upper bound on the amount of propagation that could go undetected, although because of uncertainties in image analysis Walker et al. (2015) uses a great uncertainty of 1 km, which I adopt here.

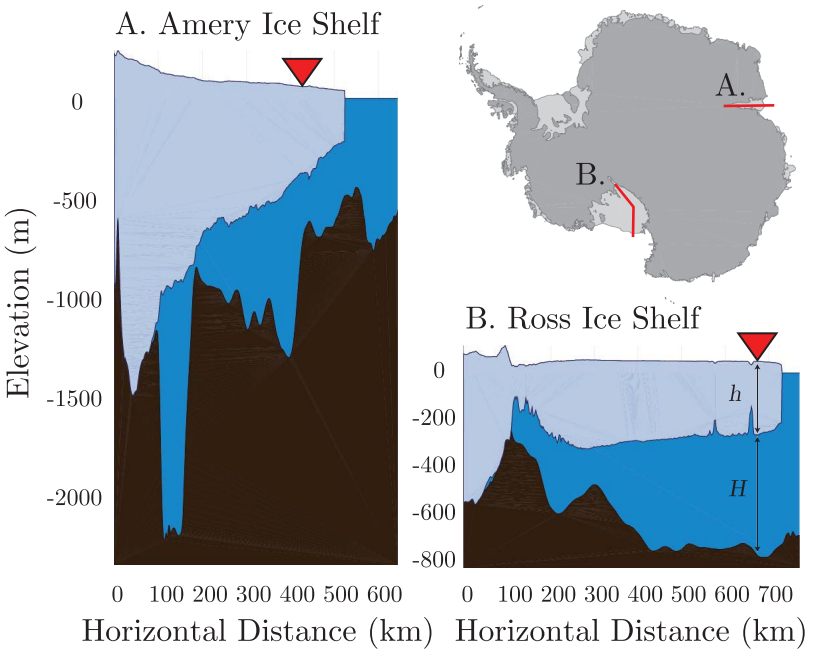

Figure 1. Profiles showing the geometry of the (a) Amery and (b) Ross. Ice Shelves and their position within the Antarctic Ice Sheet. The red triangles mark the locations of the two seismometers used in this study. The two cross sections are drawn at the same scale to emphasize geometrical differences between the two ice shelves.

4.2. Seismic Data

I analyze continuously recorded seismograms from seismometers on the Ross and Amery Ice Shelves, Antarctica. These data sets were previously described by MacAyeal et al. (2006) and Cathles et al. (2009) and by Bassis et al. (2008), respectively. I obtain all seismograms from the Incorporated Research Institutions for Seismology (IRIS) Data Management Center website. The locations of the seismometers used in this study are shown in Figure 1.

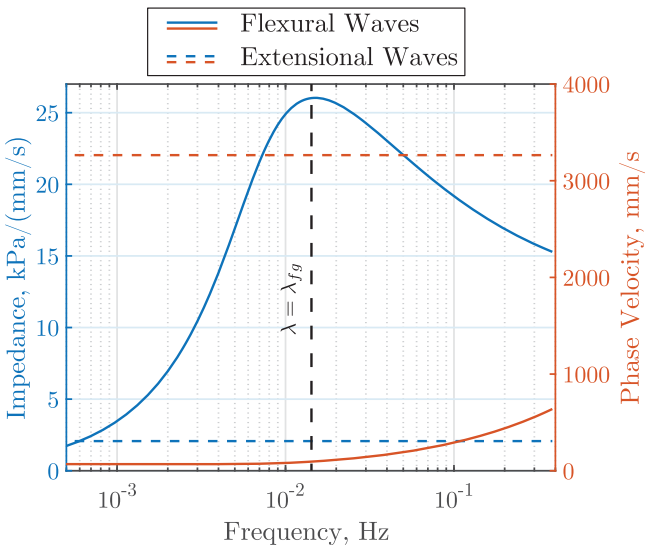

Figure 2. Wave speeds and impedances for extensional waves (dashed lines) flexural-gravity waves (solid lines). For the flexural-gravity waves, the curves are calculated for subshelf cavity thickness $H = 466$ m and ice thickness $h = 265$ m. All curves are drawn until $hk = 1/2$, reflecting the long wavelength approximation.

On the Ross Ice Shelf I examine data from the station RIS2, temporary network code XV, during the 2005–2006 deployment (MacAyeal et al., 2006). RIS2 was located several km from the tip of the Nascent Rift. From this deployment, there are 167 d of data with one outage of several days in late March 2006. On the Amery Ice Shelf I examine data from the station BFN1, temporary network code X9, during a deployment in January 2007. From this deployment there are 36 d of data. Although many other instruments were deployed over a period of several years, I focus on this station because it uses a Guralp CMG-40T seismometer while most other stations use Mark Products L28 seismometers. The CMG-40T has a flat instrumental response down to 0.03 Hz and is therefore expected to be better suited for measuring ocean waves with typical periods of several seconds.

Inferring stresses from seismograms requires interpreting the amplitude information contained in seismic traces. The issue of instrumental response therefore requires special attention. Seismometers have reduced sensitivity to motions below the instrumental sensitivity frequency. When the instrument response is deconvolved from a discretized voltage trace (with units of counts), this insensitivity results in division by a small number, thereby amplifying small amounts of noise. Although geophysically interesting information may be contained at frequencies lower than the instrumental sensitivity frequency, in this study I take a conservative approach and only interpret features in

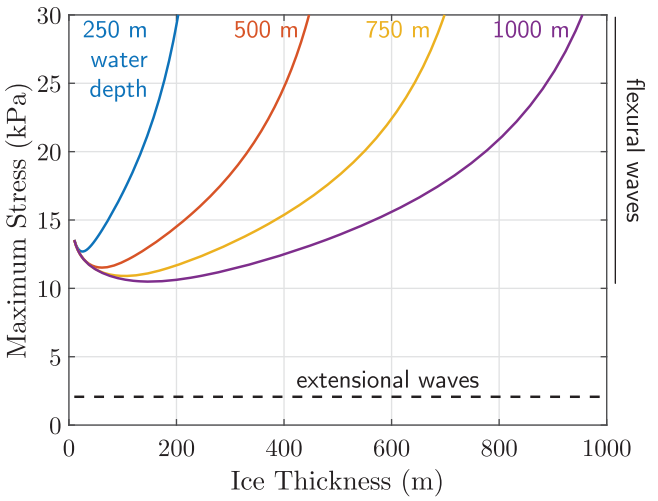

Figure 3. Maximum ice shelf stresses generated in response to waves with 0.5 mm/s particle velocity amplitude. To simulate the effect of ice shelf thinning, curves are calculated for constant ocean floor depth $H+(\rho/\rho_w)h$ but variable ice thickness h. Stresses refer to the bending stress for flexural waves and the extensional stress for extensional waves. The maximum stress is calculated for each geometry over all wavelengths λ. The highest flexural wave stress occurs for waves with wavelength λ near the flexural-gravity wavelength λ_{fg} (see Figure 2a).

seismograms that occur at frequencies above the sensitivity frequency. I first taper and then band-pass filter all raw seismic traces. The band-pass filter has cutoff frequencies 0.01, 0.02, 0.2, and 0.4 Hz. I then remove the instrumental response from all seismograms. In all of my analysis I focus on the LH channels that are sampled at 1 Hz.

Spectrograms of the waveforms used in this study shown in the spectrogram in Figure 4. The principal feature is the arrival of ocean swell from distant storms. These storm waves appear as upward sloping spectral lines. This occurs because long period ocean swell travels faster and therefore arrives before short period swell (Munk et al., 1963). This signal has been described extensively by Cathles et al. (2009) and the interested reader is referred there for more details.

5. Analysis of Seismic Data From the Ross and Amery Ice Shelves

5.1. Wave-Induced Stresses

Using the data described in section 4.2, I estimate flexural stresses σ_f using equation (7) and extensional stresses σ_e using equation (11). There are two primary results (Figure 5). First, wave stresses are much greater on the Ross Ice Shelf than on the Amery Ice Shelf. Second, on both the Amery and the Ross Ice Shelf, flexural waves carry greater stresses than extensional waves. These two patterns are true of the peak stresses as well as the root mean squared (RMS) averaged stresses. The largest observed flexural and extensional stresses on the Ross Ice Shelf were 14.2 and 0.8 kPa, respectively. On the Amery Ice Shelf, the largest observed flexural and extensional stresses were 2.1 and 0.09 kPa, respectively. The RMS flexural and extensional stresses on the Ross Ice Shelf were 0.6 and 0.03 kPa. The RMS flexural and extensional stresses on the Amery were 0.2 and 0.01 kPa.

The most likely reason for the higher observed wave stresses on the Ross Ice Shelf compared to the Amery is that the Ross seismograms are much longer (167 d) than the Amery seismograms (36 d) and were therefore able to record a wider range of variability in ocean wave activity. To test this hypothesis, I examine the most quiet period during the Ross deployment, December 2005. I refer to this as the Ross quiet period. I find that the wavefield stresses during the Ross quiet period were similar to those on the Amery Ice Shelf. During the Ross quiet period, the maximum inferred flexural and extensional stresses were 2.0 and 0.13 kPa, respectively.

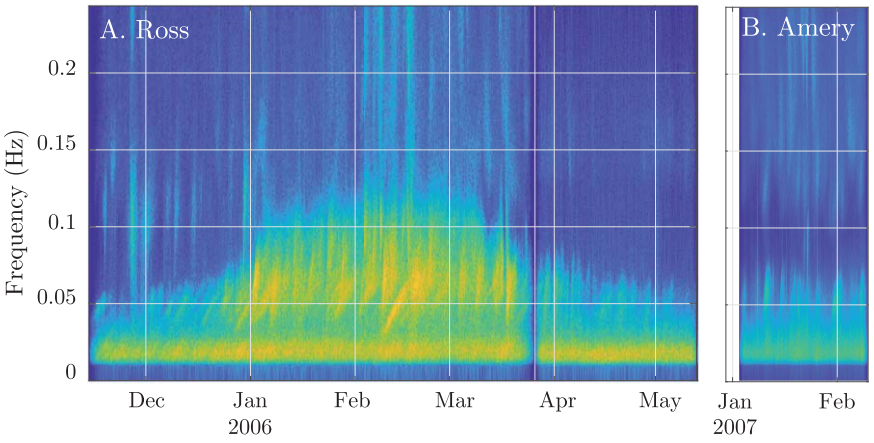

Figure 4. Spectrogram of the data from the (a) Ross and (b) Amery. Ice Shelves. Upward sloping spectral bands show the arrival of ocean swell from distant storms (Cathles et al., 2009). Both data sets are plotted with the same log-power color scale.

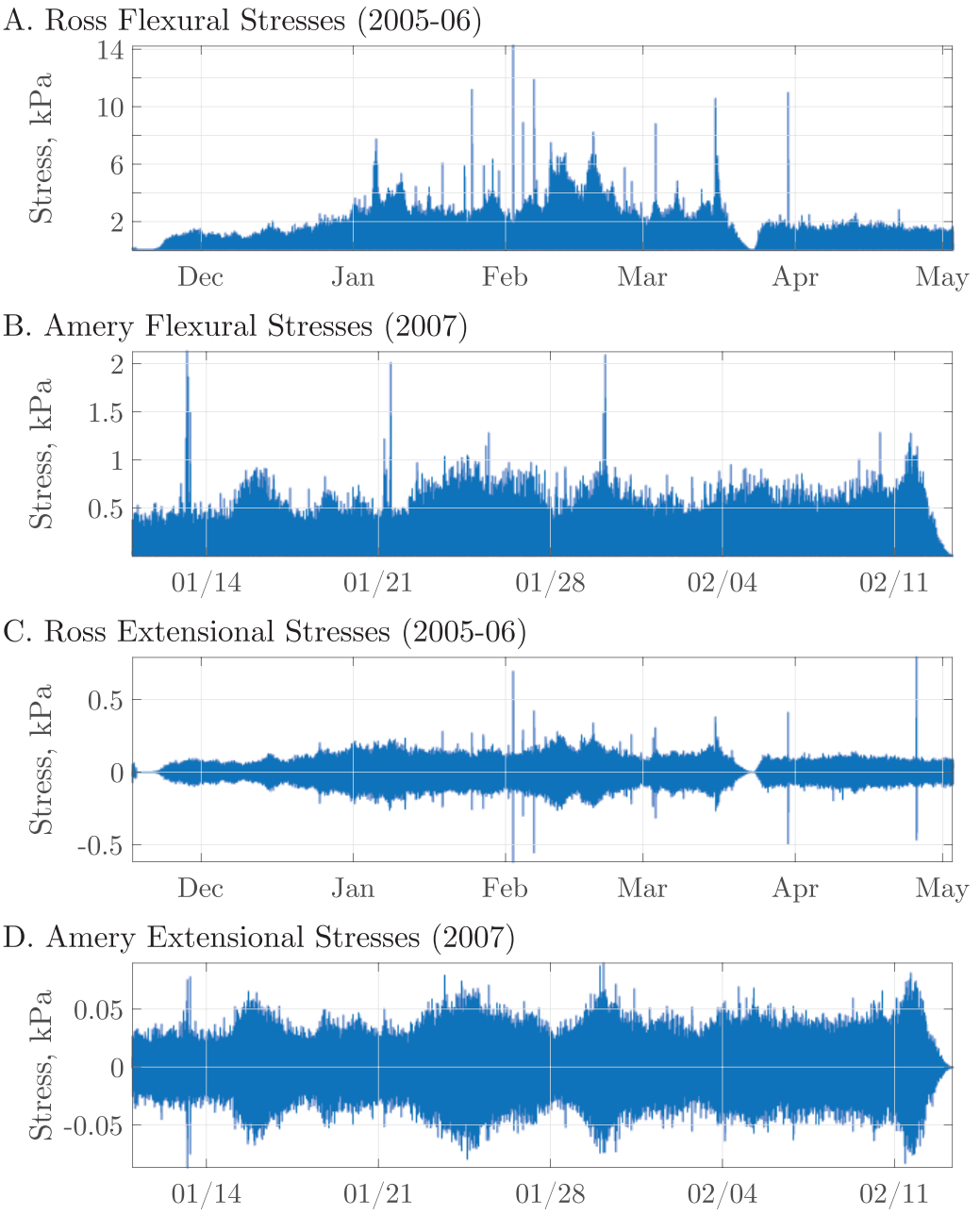

Figure 5. Calculated wave stresses on the Ross and Amery Ice Shelves. Note the different horizontal and vertical axes.

Flexural waves carried greater stresses than extensional waves during the two observation periods. The Ross Ice Shelf wave field had extensional waves with greater particle velocity amplitude than flexural wave particle velocity amplitude by a factor of three (Bromirski et al., 2010, 2015, 2017). These two waves, however, have different wave impedances. As a result, the larger stress need not be caused by the larger particle velocity.

5.2. Rift Propagation

Using the estimated stresses, I calculate the stress intensity factor K using equation (13). There are two main results. The first result is that waves stresses were exceeded the fracture criterion on the Ross Ice Shelf but not on the Amery Ice Shelf (Figure 6). As discussed later (section 6.4), I assume a fracture toughness $K_c = 400$ kPa$\sqrt{\text{m}}$ to represent tough suture zones with accreted basal marine ice. With this fracture toughness, I predict that rift propagation was possible for a cumulative total of $\sim 10^4$ s during the Ross Ice Shelf observation

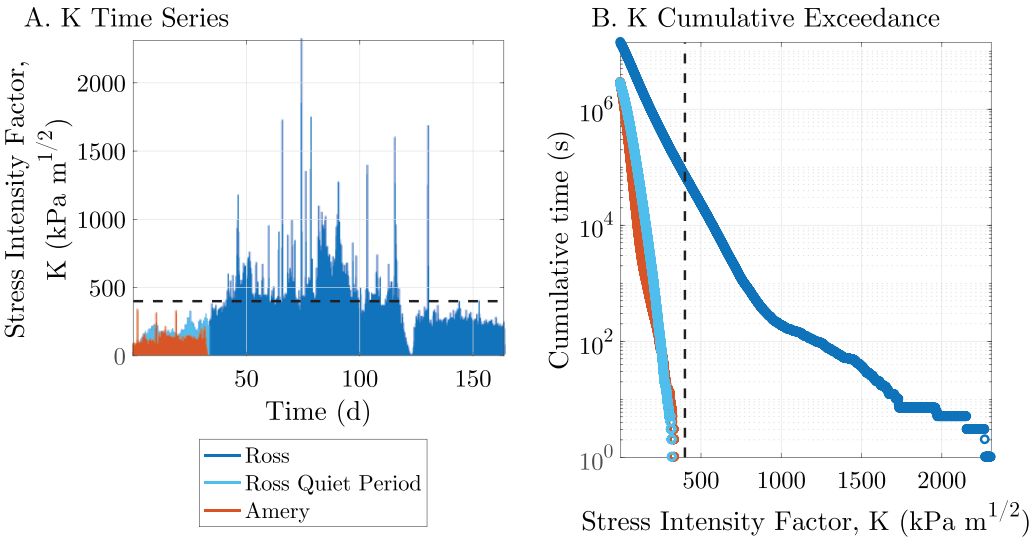

Figure 6. Comparison of the wave-induced stress intensity factor on the Ross (blue) and Amery (red) Ice Shelves. During the time of minimal wave activity on the Ross Ice Shelf (light blue), wave stresses were comparable to those observed on the Amery Ice Shelf. The stress intensity factor was computed from seismograms using equation (13) and does not account for cohesive strengthening (section 5.3). The dashed lines shows the fracture toughness K_c and therefore the value of the stress intensity factor K at which rift propagation is predicted to occur.

period. On the Amery Ice Shelf and during the quiet period on the Ross Ice Shelf, I predict that wave stresses were not large enough to induce propagation.

The second result is that, in the absence of any other resistance to rift propagation, the inferred wave-induced stresses are predicted to have caused much more propagation than was actually observed. I use the integral in equation (19) to calculate rift tip propagation distances. On the Ross Ice Shelf, a fracture toughness $K_c = 400$ kPa$\sqrt{\text{m}}$ results in a physically unrealistic 10^6 km of rift tip propagation. Actual rift propagation was measured to have been less than 1 km during the observation period (section 4). Motivated by this discrepancy, I next consider several possible sources of resistance to ice shelf rift propagation.

5.3. Rift Cohesive Strength

In order to match the observed lack of rift propagation, I consider two additional types of rift strength. First, I consider the situation discussed by Bassis et al. (2007) where the fracture toughness experiences an increase by an amount Δ to a new value $K_c+\Delta$. This perturbed value could equally well represent fracture toughness variation in space or in time. Returning to the calculation in the previous section, I find that a value of $\Delta = 1{,}600$ kPa$\sqrt{\text{m}}$ is necessary to match the observation that less than 1 km of propagation occurred. This value results in a total ice fracture toughness $\sim$2 MPa$\sqrt{\text{m}}$, which is an order of magnitude higher than typical laboratory-derived values (Rist et al., 2002). For this reason, I consider variable fracture toughness to not be a viable mechanism to explain the observed rift behavior.

As a second strengthening mechanism, I consider the cohesive effect of refrozen melange and sea ice between the rift walls. The stress intensity factor due to a uniformly applied stress acting to resist rift opening is the same as in equation (14) but with opposite sign (Sih, 2012),

$$K_{\text{cohesion}} = -\sigma_c \sqrt{\pi L/2}, \tag{20}$$

where σ_c is defined here to be the stress due to cohesive melange and sea ice that act to "glue" the rift walls together. Equation (13) then becomes,

$$K \approx \max\left[K_{\text{extension}} + K_{\text{flexure}} + K_{\text{cohesion}}, 0\right]. \tag{21}$$

The maximum function is applied because the cohesive strength does not result in a negative stress intensity factor K. A negative K would imply closing motion of the rift walls. Instead, a cohesive stress is generated only in response to wave stresses and therefore never results in negative K.

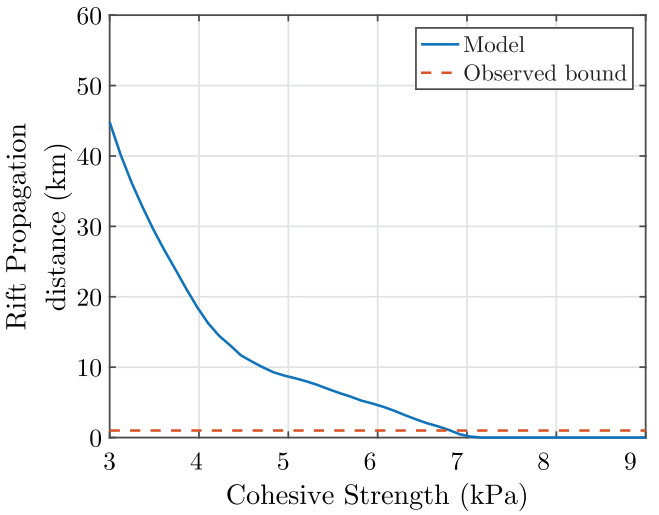

Figure 7. The predicted rift propagation decreases as the rift cohesive strength increases. Satellite imagery shows less than 1 km of propagation, therefore suggesting a cohesive strength of 6.8 kPa. The blue curve was calculated using equations (19) and (21).

I find that a cohesive stress σ_c=6.8 kPa is the minimum required cohesive stress necessary to produce $\delta L < 1$ km. This result is plotted in Figure 7, which plots the predicted amount of rift propagation as a function of the cohesive strength of the rift. In the section 6.5, I discuss several interpretations of this cohesive stress.

6. Discussion and Conclusions

6.1. Uncertainties in the Calculation of Wave-Induced Stresses

I have calculated ice shelf stresses from seismic data and related these stresses to a fracture criterion. Although I have made several simplifying assumptions, the stresses that I estimate are nevertheless in reasonable agreement with previous studies. Sergienko (2017), for example, used the BEDMAP2 geometry from the Ross Ice Shelf but employing an idealized wave forcing, calculated flexural stresses in the range of 0–15 kPa. In comparison, I find a RMS and peak wave stress on the Ross Ice Shelf of 0.8 and 17.5 kPa. The principal differences from the results of Sergienko (2017) are related topographic focusing. I treat a simplified two-dimensional geometry where the ice shelf is infinitely long and wide, small ice shelves of comparable dimension to the flexural-gravity length scale are expected to significantly deviate from the predictions made in this paper. One reason for this is that tidal stresses, for example, become significant within a distance from the grounding line that scales with λ_{fg} (Holdsworth, 1969; Vaughan, 1995).

6.2. Can Ocean Waves Trigger Rift Propagation?

To the best of my knowledge, no previous study has definitively demonstrated that ocean waves may trigger ice shelf rift propagation. To address this situation, I have attempted in this paper to construct a simple model of wave-induced rifting. Although I have been able to make this model behave in a manner consistent with observed rift behavior, no large rift propagation event occurred during the period from which I have data. As a result, definitive proof of ocean wave triggering remains elusive. This result emphasizes the importance of ongoing seismological fieldwork on ice shelves (Banwell et al., 2017; Bromirski et al., 2017). Additional fieldwork would clarify other issues as well. Although I show that a period of low wave activity on the Ross is comparable to the Amery record, further observations are needed to confirm whether activity on the Amery—or any other ice shelf for that matter—ever reaches stress levels as high as those observed on the Ross.

6.3. Other Mechanisms of Episodic Rift Extension

Larour et al. (2004a), citing laboratory studies such as those by DeFranco and Dempsey (1994), invokes constitutive instability as a possible mechanism for episodic rift activity. Constitutive instability gives rise, for example, to the stick-slip instability that is responsible for basal stick-slip motion of glaciers and ice sheets (Lipovsky & Dunham, 2016, 2017). Such behavior is a typical pathology of laboratory experiments conducted on samples which are too thin to achieve a state of plane strain (Bažant, 1993; Broek, 2012). As discussed in section 3, ice shelf rifts are expected to occur in ice that is thick enough to be in plane strain. This type of behavior is therefore expected to occur in thinner bodies of floating ice such as sea ice (DeFranco & Dempsey, 1994). Furthermore, a constitutive instability hypothesis is appealing in situations such as the tectonic earthquake cycle where the loading applied to a system is known to be approximately constant in time. The finding from the present study, that wave-induced loading is highly time dependent, suggests that constitutive instability, though possible, is not a strictly necessary condition to explain episodes of ice shelf rift propagation.

6.4. The Fracture Toughness of Ice Shelf Suture Zones

I have chosen a value $K_c = 400$ kPa$\sqrt{\text{m}}$ to represent the fracture toughness of ice shelf suture zones. This choice is based on the best available laboratory data (Rist et al., 2002), and was chosen to be at the high end of laboratory data to reflect the fact that suture zones appear to be more resistant to rift propagation

than the surrounding ice shelf (Holland et al., 2009; Jansen et al., 2013; LeDoux et al., 2017; McGrath et al., 2012). I also invoke the laboratory measurements to support the claim that fracture toughness variations cannot entirely be responsible for the observed response of the Nascent Iceberg Rift to wave-induced stresses. An important caveat to these statements is that, to my knowledge, no ice core has ever been collected from an ice shelf suture zones. Fracture toughness measurements from in situ suture zone ice cores could therefore support or refute these ideas. The exact micromechanical processes that result in the apparently elevated fracture tough of ice shelf suture zones remain unknown (McGrath et al., 2014).

6.5. Cohesive Rift Strengthening

My description of rift propagation mechanics predicts that wave stresses would have caused calving of a tabular iceberg in the absence of additional sources of rift strength. Previous studies have suggested a role for melange dynamics as a rift strengthening mechanism (Fricker et al., 2005; Larour et al., 2004b; MacAyeal et al., 1998; Rignot & MacAyeal, 1998). For simplicity, I have quantified this stabilizing tendency as a force applied uniformly over the entire rift length. This rift strengthening can equivalently be thought of as a cohesive zone (Rice, 1968). I have not attempted to quantify the spatial variation of rift strengthening; it may be the case that rift strengthening is localized to the near-tip region (Barenblatt, 1962; Dugdale, 1960). Near-tip localization of cohesive strength to a process-zone region (Broek, 2012) could result from the effect of bottom crevasses forming ahead of the rift tip (Rice & Levy, 1972) or because of rift tip blunting (Larour et al., 2004b).

6.6. Response to Melange and Ice Shelf Thinning

The rift model presented here suggests at several possible effects related to ice shelf and melange thinning. First, the result of section 5.3 suggests that rift-filling melange may stabilize rift propagation. Reduced melange may therefore weaken ice shelves by destabilizing rift propagation (MacAyeal et al., 1998; Rignot & MacAyeal, 1998). The wave response to thinning, in contrast, is stabilizing. Stabilization occurs for two reasons. First, the flexural-gravity wavelength (equation (5)) is expected to decrease. This results in a lower stress concentration due to flexural waves (equation (15)). Second, the flexural wave impedance is a increasing function of ice thickness (Figure 3). Thus thinning of an ice shelf is expected to lower wave stresses. Both of these stabilizing effects occur because thin ice shelves are more compliant and more compliant structures are less susceptible to brittle fracture. Further observations, both seismic and remotely sensed, are need to quantify whether the destabilization due to melting and warming is greater than the stabilization due to thinning.

6.7. The Loose Tooth Rift: Stabilization Due to Propagation Into Deeper Water?

The location where the Loose Tooth T2 Rift intersects the ice front, i.e., where the rift initiated, occurs in a part of the shelf that is above shallow water ($H = 253$ m). The rift has subsequently propagated into a part of the shelf that is above deeper water ($H = 466$ m). The ice thickness at the front is similar to the ice thickness at the current rift tip ($h = 265$ m versus $h = 301$ m). Carrying out a calculation of maximal flexural stress similar to Figure 3, I find that waves with identical particle velocity amplitudes would induce stresses approximately 27% higher at the ice front versus the current rift tip. Observed wave-induced stresses on the Amery were very near the failure criterion (Figure 6b). This result suggests that the Loose Tooth T2 Rift was more susceptible to wave-induced stresses during its initial formation in shallow water, and that propagation into deeper water may have stabilized the rift tip in its current position. As noted above, this hypothesis is not strictly testable because there were no seismometers deployed on the Amery during the initial formation of the Loose Tooth T2 Rift. Future seismic deployments would therefore be useful because they could clarify whether stabilization due to propagation into deeper water is an important process.

7. Conclusions

I propose a simple rift propagation criterion based on the observation that most ice shelf rifts show extended periods of dormancy and therefore must have low background stress concentrations. This low background stress concentration makes ice shelf rifts susceptible to wave-induced stresses. I infer that a cohesive strengthening of the rift, possibly due to refrozen melange, counteracts this destabilizing tendency. I relate this description of rift propagation to in situ ice shelf stresses inferred using passive seismology. By inferring stresses associated with rift propagation, this work addresses a basic limitation in our

understanding glacier calving physics: specifically, knowledge of the state of stress at the site of fracture (Benn et al., 2007). This study therefore offers a detailed glimpse into the mechanics of a particular type of glacier calving, ice shelf rift propagation.

Appendix A: Governing Equations

The propagation of ocean waves in floating ice shelves has received extensive treatment. The flexural motions of an elastic bar were first examined by Greenhill (1886). This analysis was generalized to extensional motions by Press and Ewing (1951, but see also literature cited therein). The main reason that I repeat the analysis of Press and Ewing (1951) is to obtain self-consistent expressions for the particle velocities, stresses, and dispersion relations that were not explicitly given by Press and Ewing (1951).

A1. The Elastic Ice Layer

I consider a coordinate system with the z direction being positive upward and x being positive in the direction of ice flow. An ice layer that is initially at rest and everywhere at overburden pressure occupies the region between $z=0$ and $z=-h$. The entire geometry is assumed to be translationally invariant in the x direction, and I take $u_y=\partial/\partial y=0$ so that deformations are in a state of plane strain. Perturbations to this initial state obey the momentum balance equations,

$$\rho\frac{\partial^2 u_x}{\partial t^2}=\frac{\partial \sigma_{xx}}{\partial x}+\frac{\partial \sigma_{xz}}{\partial z}, \tag{A1}$$

$$\rho\frac{\partial^2 u_z}{\partial t^2}=\frac{\partial \sigma_{xz}}{\partial z}+\frac{\partial \sigma_{zz}}{\partial z}, \tag{A2}$$

for ice density ρ and stress tensor σ_{ij}. Stresses are related to displacement gradients through the constitutive relationship (Malvern, 1969),

$$\sigma_{ij}=\lambda\left(\frac{\partial u_k}{\partial x_k}\right)\delta_{ij}+\mu\left(\frac{\partial u_i}{\partial x_j}+\frac{\partial u_j}{\partial x_i}\right), \tag{A3}$$

where, for simplicity, elastic anisotropy is neglected. The values of elastic moduli, here written using Lamé's parameter λ and the shear modulus μ, are given in Table 1.

Applying the transform of equation (2) to the governing equations (equations (A1–A3)) gives rise to a system of two coupled ordinary differential equations with derivatives in z. These equations have solution (Graff, 2012),

$$U_x=ik(A\sin\alpha z+B\cos\alpha z)+i\beta(C\cos\beta z-D\sin\beta z), \tag{A4}$$

$$U_z=\alpha(A\cos\alpha z-B\sin\alpha z)+k(C\sin\beta z+D\cos\beta z), \tag{A5}$$

where

$$\alpha=k\sqrt{\left(\frac{\omega}{kc_p}\right)^2-1}, \tag{A6}$$

$$\beta=k\sqrt{\left(\frac{\omega}{kc_s}\right)^2-1}. \tag{A7}$$

Here c_p and c_s are the P and S wave speeds in the ice (see Table 1). The quasi-static limit occurs when $\omega/(kc_p)\ll 1$ and $\omega/(kc_s)\ll 1$. In this case, $\alpha\approx\beta\approx k$.

The boundary conditions at the ice-atmosphere boundary $z=0$, are

$$\sigma_{xz}(z=0)=0, \tag{A8}$$

$$\sigma_{zz}(z=0)=0. \tag{A9}$$

Two other boundary conditions are required, and these occur at the ice-ocean interface.

A2. Ice-Ocean Coupling

The unperturbed ice-ocean interface is located at $z=-h/2$. The ice-ocean boundary moves in response to perturbations, with the deformed interface located at

$$z=-h+\phi(x,t). \tag{A10}$$

Consistent with a linearized theory of wave propagation, I assume that such geometric changes are small and following standard treatments (Gill, 2016; Lipovsky & Dunham, 2015) I prescribe boundary conditions on the undeformed interface. At this boundary, the force exerted on the ice by the water $\delta p(x,t)$ is equal and opposite to the force exerted by the water on the ice σ_{zz},

$$\sigma_{zz}(-h)=-\delta p(x,t). \tag{A11}$$

The ocean is treated as invicid so there is no shear stress,

$$\sigma_{xz}(-h)=0. \tag{A12}$$

And by continuity the velocities must match between the fluid and solid,

$$\frac{\partial u_z}{\partial t}(-h)=v_z, \tag{A13}$$

where v_z is the vertical fluid velocity. I next examine motions in the subice ocean waters with the goal of describing the fields δp and v_z (equations (A11) and (A13)) on the ice-ocean interface.

A3. Subice-Shelf Cavity Circulation

I examine the behavior of perturbations to a subice-shelf cavity initially at rest. In this initial state, the pressure in the water is,

$$p_0(z)=\rho_w g(z+h)+\rho g h. \tag{A14}$$

I then define the total fluid pressure p' to be

$$p'(x,z,t)=p(x,z,t)+p_0(z) \tag{A15}$$

Flow perturbations follow the linearized equations for an incompressible, inviscid flow with uniform density. The horizontal and vertical momentum balance equations are

$$\rho_w \frac{\partial v_x}{\partial t}=-\frac{\partial p}{\partial x}, \tag{A16}$$

$$\rho_w \frac{\partial v_z}{\partial t}=-\frac{\partial p}{\partial z}. \tag{A17}$$

Here v_x and v_z are the x and z components of fluid velocity.

I assume that the ocean waters are of uniform density so that the ocean water mass conservation equation is

$$\frac{\partial v_x}{\partial x}+\frac{\partial v_z}{\partial z}=0. \tag{A18}$$

This statement of mass conservation may be combined with equations (A16) and (A17) with the result being Laplace's equation for pressure,

$$\nabla^2 p=0. \tag{A19}$$

The fluid flow is irrotational as a consequence of the inviscid, uniform density, and small perturbation assumptions (Gill, 2016, section 5.2).

The boundary condition at the ocean bottom, $z=-h-H$, is that vertical velocities vanish,

$$v_z(z=-h-H)=0. \tag{A20}$$

At the ice-ocean interface, the water pressure perturbation is approximately equal to the hydrostatic pressure at the deformed ice-ocean interface location ϕ plus the pressure exerted by the ice on the water,

$$p(-h)=\rho_w g\phi(x,t)+\delta p(x,t). \tag{A21}$$

The fluid equations (A19–A21) may be solved in the transform domain using equation (2). The result is a transfer function between ΔP and surface height Φ,

$$\Delta P=\rho_w g\left(\frac{\omega^2}{gk}\coth(kH)-1\right)\Phi \equiv -T(k,\omega)\Phi. \tag{A22}$$

I again apply the convention from the main text that capital letters denote Fourier transformed quantities.

The transfer function of equation (A22), combined with the ice-ocean coupling conditions (equations (A11) and (A13)), allows me to write the entire coupled ice-ocean problem exclusively in terms of boundary conditions on the elastic solid. In equation (A22), ΔP and Φ can be eliminated in favor of the field variables Σ_{zz} and U_z, defined in the elastic solid. The result is the bottom boundary conditions on the elastic ice layer,

$$\Sigma_{zz}(z=-h)=T(k,\omega)U_z(z=-h), \tag{A23}$$

$$\Sigma_{xz}(z=-h)=0. \tag{A24}$$

It is interesting to note that ice-ocean coupling manifests itself as the condition in equation (A23), namely, as a Robin type boundary condition that relates the vertical elastic displacement to the vertical compressive elastic stress.

A4. The Dispersion Relation

The four boundary conditions (equations (A8), (A9), (A23), and (A24)) on the elastic solid result in a homogeneous system of equations,

$$\left\{\begin{bmatrix} 2\left(k^2-\beta^2\right)\mu\cos(h\alpha) & 4k\beta\mu\cos(h\beta) & 0 & 0 \\ 2k\alpha\sin(h\alpha) & \left(\beta^2-k^2\right)\sin(h\beta) & 0 & 0 \\ 0 & 0 & 4k\beta\mu\sin(h\beta) & 2\left(\beta^2-k^2\right)\mu\sin(h\alpha) \\ 0 & 0 & \left(k^2-\beta^2\right)\cos(h\beta) & 2k\alpha\cos(h\alpha) \end{bmatrix} -T\begin{bmatrix} \alpha\sin(h\alpha) & -k\sin(h\beta) & k\cos(h\beta) & \alpha\cos(h\alpha) \\ 0 & 0 & 0 & 0 \\ \alpha\sin(h\alpha) & -k\sin(h\beta) & k\cos(h\beta) & \alpha\cos(h\alpha) \\ 0 & 0 & 0 & 0 \end{bmatrix}\right\}\begin{pmatrix} B \\ C \\ D \\ A \end{pmatrix}=\begin{pmatrix} 0 \\ 0 \\ 0 \\ 0 \end{pmatrix} \tag{A25}$$

Solutions to these equations require a vanishing determinant, and this condition gives rise to the dispersion relation,

$$D(k,\omega)=D_E(k,\omega)D_F(k,\omega)+D_{HD}(k,\omega)=0. \tag{A26}$$

where

$$D_F \equiv \frac{\tan(\alpha h)}{\tan(\beta h)}+\frac{\left(k^2-\beta^2\right)^2}{4\alpha\beta k^2}, \tag{A27}$$

$$D_E \equiv \frac{\tan(\alpha h)}{\tan(\beta h)}+\frac{4\alpha\beta k^2}{\left(k^2-\beta^2\right)^2}, \tag{A28}$$

$$D_{HD} \equiv \frac{T}{2\mu}\frac{\alpha\left(\beta^2+k^2\right)\left[\tan^2(\alpha h)-1\right]}{4\alpha\beta k^2\tan(\beta h)}\left[\frac{\tan^2(\beta h)-1}{\tan^2(\alpha h)-1}+\frac{\tan(\alpha h)}{\tan(\beta h)}\frac{4\alpha\beta k^2}{\left(k^2-\beta^2\right)^2}\right]. \tag{A29}$$

The subscript *HD* stands for hydrodynamic. Terms with this subscript are related to flow in the subshelf cavity.

When ice-ocean coupling is absent, $T = 0$ and so $D_{HD} = 0$. In this case, equation (A26) reduces to the Lamb wave dispersion relation. This dispersion relation corresponds to the motions of an elastic layer with zero stress boundary conditions (Graff, 2012). The Lamb wave dispersion relation is notable because it consists of uncoupled flexural and extensional modes. Mathematically this uncoupling occurs because it is possible to factor the dispersion relation into the product of two terms, D_E and D_F. Equation (A26) is equivalent to equation (49) of Wang and Shen (2010) in the case of a perfectly elastic ice layer.

In general, the mechanical interaction that occurs at the ice-ocean interface results in coupling between the flexural and extensional motions of the ice shelf. For this reason, there are no longer uncoupled flexural and extensional modes over the entire frequency-spectra and wave number-spectra as there is in the more specific Lamb wave case. I will show in the next section, however, that for wavelengths that are long compared to the ice thickness, a simplification to extensional and flexural modes occurs.

Appendix B: The Long Wavelength Limit

The observed seismic spectrum on the Ross and Amery Ice Shelves is dominated by wave energy at frequencies lower than several seconds (Figure 4). Using the dispersion relations for extensional (equation (9)) and flexural wave motions (equation (4)), I calculate that these waves correspond to waves with wavelength of at least several kilometers. This observation motivates a more careful examination of waves with wavelength that are much longer than the ice shelf thickness. I calculate the Taylor series in the small parameter kh for the dispersion relation of equation (A26),

$$D_F \approx \frac{1}{12}\left(\frac{\omega}{kc_s}\right)^2\left\{\frac{\omega^2}{c_s^2k^2}\left[\frac{1}{2}\left(\gamma^2-1\right)^2h^2k^2-3\right]+\left(\gamma^2-1\right)h^2k^2\right\}, \tag{B1}$$

$$D_E \approx \frac{1}{4}\left(\frac{\omega}{kc_s}\right)^2\left[4\left(\gamma^2-1\right)+\left(2\gamma^4-1\right)\frac{\omega^2}{c_s^2k^2}\right], \tag{B2}$$

$$D_{HD} \approx \frac{T}{\mu hk^2}\frac{1}{4}\left(\frac{\omega}{kc_s}\right)^4\left[4\left(\gamma^2-1\right)+\left(2\gamma^4-1\right)\frac{\omega^2}{c_s^2k^2}\right]\left[\frac{\gamma^2+1}{2}\frac{\omega^2}{k^2c_s^2}+1\right]. \tag{B3}$$

I have defined $\gamma \equiv c_s/c_p$. The resulting expression for the dispersion relation permits factorization into the form,

$$\begin{aligned} D(k,\omega) \approx{}& \left(\frac{\omega}{c_sk}\right)^4\left\{4\left(\gamma^2-1\right)+\left(2\gamma^4-1\right)\left(\frac{\omega}{c_sk}\right)^2\right\} \\ &\times\left\{\left(\gamma^2-1\right)h^2k^2+\frac{3T}{h\mu k^2}\left[\frac{\gamma^2+1}{2}\left(\frac{\omega}{c_sk}\right)^2+1\right]\right. \\ &\left.+\left[\frac{1}{2}\left(\gamma^2-1\right)^2h^2k^2-3\right]\left(\frac{\omega}{c_sk}\right)^2\right\}, \end{aligned} \tag{B4}$$

which has the property that it consists of two uncoupled modes.

The first mode, corresponding to the first curly bracketed term, is identical to the long wavelength symmetric Lamb wave mode. Its phase velocity is given by equation (9).

The second mode, corresponding to the second curly bracketed term, is a modification of the long wavelength antisymmetric Lamb wave mode. The dispersion relation for this mode is,

$$\left(1-\gamma^2\right)h^2k^2+\frac{3T}{h\mu k^2}\left[\frac{\gamma^2+1}{2}\left(\frac{\omega}{c_sk}\right)^2+1\right]+\left[\frac{1}{2}\left(\gamma^2-1\right)^2h^2k^2-3\right]\left(\frac{\omega}{c_sk}\right)^2=0. \tag{B5}$$

Keeping only the lowest order terms in the small parameter kh gives

$$Dk^4-h\rho\omega^2=-T, \tag{B6}$$

where $D \equiv \mu(1-\gamma^2)h^3/3$ is the flexural rigidity, which is equivalent to another commonly used expression, $Eh^3/[12(1-\nu^2)]$.

I have not yet made use of the ice-ocean transfer function. The results in this section up to this point are therefore valid for any ice-ocean transfer function T. Using the transfer function T from equation (A22) then gives the dispersion equation of equation (4).

Appendix C: Wave Particle Motions

I calculate particle motions by regrouping the general solution (equations (A4) and (A5)) into symmetric and antisymmetric terms. In order to highlight symmetries about the midplane of the ice layer, I define the coordinate $z' \equiv z - h/2$. The ice-atmosphere and ice-ocean surfaces are then located at $z' = \pm h$. These terms correspond to extensional and flexural motions, respectively,

$$\frac{U_x^F}{A} = ik\sin\alpha z' - i\frac{D}{A}\beta\sin\beta z', \tag{C1}$$

$$\frac{U_z^F}{A} = \alpha\cos\alpha z' + \frac{D}{A}k\cos\beta z', \tag{C2}$$

$$\frac{U_x^E}{C} = i\frac{B}{C}k\cos\alpha z' + i\beta\cos\beta z', \tag{C3}$$

$$\frac{U_z^E}{C} = -\frac{B}{C}\alpha\sin\alpha z' + k\sin\beta z'. \tag{C4}$$

The ratios D/A and B/C are defined from the zero shear stress boundary conditions at $z' = \pm h/2$, as expressed in the second and fourth lines of the matrix in equation (A25),

$$\frac{B}{C} = \frac{(k^2-\beta^2)\sin(h\beta/2)}{2k\alpha\sin(h\alpha/2)} \tag{C5}$$

$$\frac{D}{A} = \frac{2k\alpha\cos(h\alpha/2)}{(\beta^2-k^2)\cos(h\beta/2)} \tag{C6}$$

The other boundary conditions enter through the requirement that k and ω be related by the dispersion relation. In the long wavelength limit, $B/C \approx D/A \approx -i$. The equations for particle motion (equations (C1–C6)), combined with the elastic constitutive relation (equation (A3)), suffice to calculate the impedance tensor of equation (1).

Extensional waves have particle motions,

$$\frac{U_x^E}{C} \approx -2k, \tag{C7}$$

$$\frac{U_z^E}{C} \approx 2i(kz')k. \tag{C8}$$

I note that the long wavelength limit $kh \ll 1$ is distinct from the quasi-static limit where $\omega/(kc_p) \ll 1$. In other words, long wavelength extensional waves are not quasi-static. The long wavelength extensional mode has dominantly horizontal displacements $|U_x^E|/|U_z^E| \sim (kz')^{-1}$ that are constant throughout the ice layer. The much smaller vertical displacements, in contrast, are antisymmetric about the midplane of the ice layer.

Flexural motions have phase velocity given by equation (4). The particle motions satisfy,

$$\frac{U_x^F}{A} \approx -\frac{k^2\omega^2 z'}{2\gamma^2} \tag{C9}$$

$$\frac{U_z^F}{A} \approx -\frac{ik\omega^2}{2\gamma^2} \tag{C10}$$

Unlike the extensional mode, the flexural mode long wavelength limit is also quasi-static. The long wavelength flexural mode has dominantly vertical displacements $|U_z^F|/|U_x^F| \sim (kz)^{-1}$ that are constant throughout the ice layer. The much smaller horizontal displacements, in contrast, are antisymmetric about the midplane of the ice layer.

Acknowledgments
This work was supported by a Postdoctoral Fellowship in the Department of Earth and Planetary Sciences at Harvard University. Discussions with Catherine Walker, Jim Rice, and Doug MacAyeal provided useful context for this study. Greg Wagner read an early version of this paper and provided feedback. Victor Tsai demanded better explanations. Marine Denolle asked several important questions. Olga Sergienko and an anonymous reviewer provided comments that significantly improved the quality of the manuscript. All of the data used in this study have been previously published: the seismic data are freely available at the IRIS Consortium website (http://doi.org/10.7914/SN/XV_2003 and http://doi.org/10.7914/SN/X9_2004) and the satellite imagery is available on the NSIDC website (http://nsidc.org/data/iceshelves_images/index_modis.html). Maps were made using the Antarctic mapping tools for MATLAB (Greene et al., 2017).

References

Alley, R. B., Dupont, T. K., Parizek, B. R., & Anandakrishnan, S. (2005). Access of surface meltwater to beds of sub-freezing glaciers: Preliminary insights. *Annals of Glaciology*, *40*, 8–14.

Banwell, A. F., Willis, I. C., Macdonald, G. J., Goodsell, B., Mayer, D. P., Powell, A., et al. (2017). Calving and rifting on the McMurdo Ice Shelf, Antarctica. *Annals of Glaciology*, *58*, 78–87.

Barenblatt, G. I. (1962). The mathematical theory of equilibrium cracks in brittle fracture. In H. L. Dryden & T. von Kannan (Eds.), *Advances in applied mechanics* (Vol. 7, pp. 55–129). New York, NY: Academic Press.

Bassis, J. N., Coleman, R., Fricker, H., & Minster, J. (2005). Episodic propagation of a rift on the Amery Ice Shelf, East Antarctica. *Geophysical Research Letters*, *32*, L06502. https://doi.org/10.1029/2004GL022048

Bassis, J. N., Fricker, H. A., Coleman, R., Bock, Y., Behrens, J., Darnell, D., et al. (2007). Seismicity and deformation associated with ice-shelf rift propagation. *Journal of Glaciology*, *53*(183), 523–536.

Bassis, J. N., Fricker, H. A., Coleman, R., & Minster, J.-B. (2008). An investigation into the forces that drive ice-shelf rift propagation on the Amery Ice Shelf, East Antarctica. *Journal of Glaciology*, *54*(184), 17–27.

Bažant, Z. P. (1992). Large-scale thermal bending fracture of sea ice plates. *Journal of Geophysical Research*, *97*(C11), 17739–17751.

Bažant, Z. P. (1993). Scaling laws in mechanics of failure. *Journal of Engineering Mechanics*, *119*(9), 1828–1844.

Benn, D. I., Warren, C. R., & Mottram, R. H. (2007). Calving processes and the dynamics of calving glaciers. *Earth-Science Reviews*, *82*(3), 143–179.

Borstad, C., Khazendar, A., Larour, E., Morlighem, M., Rignot, E., Schodlok, M., et al. (2012). A damage mechanics assessment of the Larsen B ice shelf prior to collapse: Toward a physically-based calving law. *Geophysical Research Letters*, *39*, L18502. https://doi/org/10.1029/2012GL053317

Borstad, C., McGrath, D., & Pope, A. (2017). Fracture propagation and stability of ice shelves governed by ice shelf heterogeneity. *Geophysical Research Letters*, *44*, 4186–4194. https://doi/org/10.1002/2017GL072648

Borstad, C., Rignot, E., Mouginot, J., & Schodlok, M. (2013). Creep deformation and buttressing capacity of damaged ice shelves: Theory and application to Larsen C ice shelf. *The Cryosphere*, *7*(6), 1931–1947.

Broek, D. (2012). *Elementary engineering fracture mechanics*. Dordrecht, the Netherlands: Springer Science & Business Media.

Bromirski, P., Chen, Z., Stephen, R., Gerstoft, P., Arcas, D., Diez, A., et al. (2017). Tsunami and infragravity waves impacting Antarctic ice shelves. *Journal of Geophysical Research: Oceans*, *122*, 5786–5801. https://doi/org/10.1002/2017JC012913

Bromirski, P. D., Diez, A., Gerstoft, P., Stephen, R. A., Bolmer, T., Wiens, D. A., et al. (2015). Ross ice shelf vibrations. *Geophysical Research Letters*, *42*, 7589–7597. https://doi/org/10.1002/2015GL065284

Bromirski, P. D., Sergienko, O. V., & MacAyeal, D. R. (2010). Transoceanic infragravity waves impacting Antarctic ice shelves. *Geophysical Research Letters*, *37*, L02502. https://doi/org/10.1029/2009GL041488

Brunt, K. M., Okal, E. A., & MacAyeal, D. R. (2011). Antarctic ice-shelf calving triggered by the Honshu (Japan) earthquake and tsunami, March 2011. *Journal of Glaciology*, *57*(205), 785–788.

Cathles, L., Okal, E. A., & MacAyeal, D. R. (2009). Seismic observations of sea swell on the floating Ross Ice Shelf, Antarctica. *Journal of Geophysical Research*, *114*, F02015. https://doi/org/10.1029/2007JF000934

DeFranco, S. J., & Dempsey, J. P. (1994). Crack propagation and fracture resistance in saline ice. *Journal of Glaciology*, *40*(136), 451–462.

Doake, C., Corr, H., Rott, H., Skvarca, P., & Young, N. (1998). Breakup and conditions for stability of the northern Larsen Ice Shelf, Antarctica. *Nature*, *391*(6669), 778–780.

Duddu, R., Bassis, J., & Waisman, H. (2013). A numerical investigation of surface crevasse propagation in glaciers using nonlocal continuum damage mechanics. *Geophysical Research Letters*, *40*, 3064–3068. https://doi/org/10.1002/grl.50602

Duddu, R., & Waisman, H. (2013). A nonlocal continuum damage mechanics approach to simulation of creep fracture in ice sheets, *Computational Mechanics*, *51*(6), 961–974.

Dugdale, D. S. (1960). Yielding of steel sheets containing slits. *Journal of the Mechanics and Physics of Solids*, *8*(2), 100–104.

Fretwell, P., Pritchard, H. D., Vaughan, D., Bamber, G., Barrand, J., Bell, N., et al. (2013). Bedmap2: Improved ice bed, surface and thickness datasets for Antarctica. *The Cryosphere*, *7*(1), 375–393.

Freund, L. (1972a). Crack propagation in an elastic solid subjected to general loading. i: Constant rate of extension. *Journal of the Mechanics and Physics of Solids*, *20*(3), 129–140.

Freund, L. (1972b). Crack propagation in an elastic solid subjected to general loading. ii: Non-uniform rate of extension. *Journal of the Mechanics and Physics of Solids*, *20*(3), 141–152.

Freund, L. B. (1998). *Dynamic fracture mechanics*. Cambridge, UK: Cambridge University Press.

Fricker, H., Young, N., Coleman, R., Bassis, J., & Minster, J.-B. (2005). Multi-year monitoring of rift propagation on the Amery Ice Shelf, East Antarctica. *Geophysical Research Letters*, *32*, L02502. https://doi/org/10.1029/2004GL021036

Gill, A. E. (2016). *Atmosphere and ocean dynamics*. New York, NY: Elsevier.

Graff, K. F. (2012). *Wave motion in elastic solids*. Mineola, NY: Courier Corporation.

Greene, C. A., Gwyther, D. E., & Blankenship, D. D. (2017). Antarctic mapping tools for MATLAB. *Computers and Geosciences*, *104*, 151–157.

Greenhill, A.-G. (1886). Wave motion in hydrodynamics. *American Journal of Mathematics*, *371*, 62–96.

Griffith, A. A. (1921). The phenomena of rupture and flow in solids. *Philosophical Transactions of the Royal Society of London, Series A*, *221*, 163–198.

Holdsworth, G. (1969). Flexure of a floating ice tongue. *Journal of Glaciology*, *8*(54), 385–397.

Holdsworth, G., & Glynn, J. (1978). Iceberg calving from floating glaciers by a vibrating mechanism. *Nature*, *274*(5670), 464–466.

Holland, P. R., Corr, H. F., Vaughan, D. G., Jenkins, A., & Skvarca, P. (2009). Marine ice in Larsen ice shelf. *Geophysical Research Letters*, *36*, L11604. https://doi.org/10.1029/2009GL038162

Hulbe, C. L., LeDoux, C., & Cruikshank, K. (2010). Propagation of long fractures in the Ronne Ice Shelf, Antarctica, investigated using a numerical model of fracture propagation. *Journal of Glaciology*, *56*(197), 459–472.

Irwin, G. R. (1957). Analysis of stresses and strains near the end of a crack traversing a plate. *Journal of Applied Mechanics*, *24*(3), 361–364.

Jacobs, S., MacAyeal, D., & Ardai, J. (1986). The recent advance of the Ross Ice Shelf Antarctica. *Journal of Glaciology*, *32*(112), 464–474.

Jansen, D., Luckman, A., Kulessa, B., Holland, P. R., & King, E. C. (2013). Marine ice formation in a suture zone on the Larsen C Ice Shelf and its influence on ice shelf dynamics. *Journal of Geophysical Research: Earth Surface*, *118*, 1628–1640. https://doi.org/10.1002/jgrf.20120

Joughin, I., & MacAyeal, D. R. (2005). Calving of large tabular icebergs from ice shelf rift systems. *Geophysical Research Letters*, *32*, L02501. https://doi.org/10.1029/2004GL020978

Keys, H. J., Jacobs, S. S., & Brigham, L. W. (1998). Continued northward expansion of the Ross Ice Shelf, Antarctica. *Annals of Glaciology*, *27*, 93–98.

Konovalov, Y. (2014). Ice-shelf resonance deflections modelled with a 2-D elastic centre-line model. *Physical Review & Research International*, *4*, 9–29.
Krawczynski, M. J., Behn, M. D., Das, S. B., & Joughin, I. (2009). Constraints on the lake volume required for hydro-fracture through ice sheets. *Geophysical Research Letters*, *36*, L10501. https://doi.org/10.1029/2008GL036765
Krug, J., Weiss, J., Gagliardini, O., & Durand, G. (2014). Combining damage and fracture mechanics to model calving. *The Cryosphere Discussions*, *8*(1), 1111–1150.
Larour, E., Rignot, E., & Aubry, D. (2004a). Processes involved in the propagation of rifts near Hemmen ice rise, Ronne ice shelf, Antarctica. *Journal of Glaciology*, *50*(170), 329–341.
Larour, E., Rignot, E., & Aubry, D. (2004b). Modelling of rift propagation on Ronne Ice Shelf, Antarctica, and sensitivity to climate change. *Geophysical Research Letters*, *31*, L16404. https://doi.org/10.1029/2004GL020077
LeDoux, C. M., Hulbe, C. L., Forbes, M. P., Scambos, T. A., & Alley, K. (2017). Structural provinces of the Ross Ice Shelf, Antarctica, *Annals of Glaciology*, *58*, 88–98.
Lemaitre, J. (1985). A continuous damage mechanics model for ductile fracture, *Journal of Engineering Materials and Technology*, *107*(1), 83–89.
Lipovsky, B. P., & Dunham, E. M. (2015). Vibrational modes of hydraulic fractures: Inference of fracture geometry from resonant frequencies and attenuation. *Journal of Geophysical Research: Solid Earth*, *120*, 1080–1107. https://doi.org/10.1002/2014JB011286
Lipovsky, B. P., & Dunham, E. M. (2016). Tremor during ice-stream stick slip. *The Cryosphere*, *10*(1), 385–399.
Lipovsky, B. P., & Dunham, E. M. (2017). Slow-slip events on the Whillans Ice Plain, Antarctica, described using rate-and-state friction as an ice stream sliding law. *Journal of Geophysical Research: Earth Surface*, *122*, 973–1003.
MacAyeal, D. R., Okal, E. A., Aster, R. C., Bassis, J. N., Brunt, K. M., Cathles, L. M., et al. (2006). Transoceanic wave propagation links iceberg calving margins of Antarctica with storms in tropics and Northern Hemisphere. *Geophysical Research Letters*, *33*, L17502. https://doi.org/10.1029/2006GL027235
MacAyeal, D. R., Rignot, E., & Hulbe, C. L. (1998). Ice-shelf dynamics near the front of the Filchner-Ronne Ice Shelf, Antarctica, revealed by SAR interferometry: Model/interferogram comparison. *Journal of Glaciology*, *44*(147), 419–428.
Malvern, L. E. (1969). *Introduction to the mechanics of a continuous medium* (Monograph). Englewood Cliffs, NJ: Prentice-Hall. Inc.
McGrath, D., Steffen, K., Holland, P. R., Scambos, T., Rajaram, H., Abdalati, W., et al. (2014). The structure and effect of suture zones in the Larsen C Ice Shelf, Antarctica. *Journal of Geophysical Research: Earth Surface*, *119*, 588–602. https://doi.org/10.1002/2013JF002935
McGrath, D., Steffen, K., Rajaram, H., Scambos, T., Abdalati, W., & Rignot, E. (2012). Basal crevasses on the Larsen C Ice Shelf, Antarctica: Implications for meltwater ponding and hydrofracture. *Geophysical Research Letters*, *39*, L16504. https://doi.org/10.1029/2012GL052413
Munk, W. H., Miller, G., Snodgrass, F., & Barber, N. (1963). Directional recording of swell from distant storms. *Philosophical Transactions of the Royal Society of London A*, *255*(1062), 505–584.
Nemat-Nasser, S., Oranratnachai, A., & Keer, L. (1979). Spacing of water-free crevasses. *Journal of Geophysical Research*, *84*(B9), 4611–4620.
Plate, C., Müller, R., Humbert, A., & Gross, D. (2012). Evaluation of the criticality of cracks in ice shelves using finite element simulations. *The Cryosphere*, *6*(5), 973–984.
Powell, A. (2015). *Frozen south: Ice breakout*. Chicago, IL: Music Box Films. Retrieved from https://vimeo.com/159039693
Pralong, A., & Funk, M. (2005). Dynamic damage model of crevasse opening and application to glacier calving. *Journal of Geophysical Research*, *110*, B01309. https://doi.org/10.1029/2004JB003104
Press, F., & Ewing, M. (1951). Propagation of elastic waves in a floating ice sheet, *Transactions American Geophysical Union*, *32*(5), 673–678.
Reeh, N. (1968). On the calving of ice from floating glaciers and ice shelves. *Journal of Glaciology*, *7*(50), 215–232.
Rice, J. R. (1968). A path independent integral and the approximate analysis of strain concentration by notches and cracks. *Journal of Applied Mechanics*, *35*(2), 379–386.
Rice, J. R. (2001). New perspectives on crack and fault dynamics. In H. Aref & J. W. Philips (Eds.), *Mechanics for a new millennium* (pp. 1–24). Dordrecht, the Netherlands: Springer.
Rice, J. R., & Levy, N. (1972). The part-through surface crack in an elastic plate. *Journal of Applied Mechanics*, *39*(1), 185–194.
Rice, J. R., & Tracey, D. M. (1969). On the ductile enlargement of voids in triaxial stress fields. *Journal of the Mechanics and Physics of Solids*, *17*(3), 201–217.
Rignot, E., Casassa, G., Gogineni, P., Krabill, W., Rivera, A., & Thomas, R. (2004). Accelerated ice discharge from the Antarctic Peninsula following the collapse of Larsen B ice shelf. *Geophysical Research Letters*, *31*, L18401. https://doi.org/10.1029/2004GL020697
Rignot, E., & MacAyeal, D. R. (1998). Ice-shelf dynamics near the front of the Filchner Ronne Ice Shelf, Antarctica, revealed by SAR interferometry. *Journal of Glaciology*, *44*(147), 405–418.
Rist, M., Sammonds, P., Oerter, H., & Doake, C. (2002). Fracture of Antarctic shelf ice. *Journal of Geophysical Research*, *107*(B1), https://doi.org/10.1029/2000JB000058
Robin, G. D. Q. (1979). Formation, flow, and disintegration of ice shelves. *Journal of Glaciology*, *24*(90), 259–271.
Scambos, T. A., Bohlander, J., Shuman, C. U., & Skvarca, P. (2004). Glacier acceleration and thinning after ice shelf collapse in the Larsen B embayment, Antarctica. *Geophysical Research Letters*, *31*, L18402. https://doi.org/10.1029/2004GL02067
Scambos, T., Bohlander, J., & Raup, B. (2009b). *Images of Antarctic ice shelves*. Boulder, CO: National Snow and Ice Data Center. Retrieved from http://nsidc.org/data/iceshelves\images
Scambos, T., Fricker, H. A., Liu, C.-C., Bohlander, J., Fastook, J., Sargent, A., et al. (2009a). Ice shelf disintegration by plate bending and hydro-fracture: Satellite observations and model results of the 2008 Wilkins Ice Shelf break-ups. *Earth and Planetary Science Letters*, *280*(1), 51–60.
Scambos, T., Haran, T., Fahnestock, M., Painter, T., & Bohlander, J. (2007). MODIS-based mosaic of Antarctica (MOA) data sets: Continent-wide surface morphology and snow grain size. *Remote Sensing of Environment*, *111*(2–3), 242–257.
Schulson, E. M., & Duval, P. (2009). *Creep and fracture of ice* (Vol. 1). Cambridge, UK: Cambridge University Press.
Sergienko, O. (2010). Elastic response of floating glacier ice to impact of long-period ocean waves. *Journal of Geophysical Research*, *115*, F04028. https://doi.org/10.1029/2010JF001721
Sergienko, O. (2013). Normal modes of a coupled ice-shelf/sub-ice-shelf cavity system. *Journal of Glaciology*, *59*(213), 76–80.
Sergienko, O. (2017). Behavior of flexural gravity waves on ice shelves: Application to the Ross Ice Shelf. *Journal of Geophysical Research: Oceans*, *122*, 6147–6164. https://doi.org/10.1002/2017JC012947
Shabtaie, S., & Bentley, C. R. (1982). Tabular icebergs: Implications from geophysical studies of ice shelves. *Journal of Glaciology*, *28*(100), 413–430.
Sih, G. C. (2012). *Plates and shells with cracks: A collection of stress intensity factor solutions for cracks in plates and shells* (Vol. 3). Dordrecht, the Netherlands: Springer Science & Business Media.

Smith, R. (1976). The application of fracture mechanics to the problem of crevasse penetration. *Journal of Glaciology*, *17*(76), 223–228.
Van der Veen, C. (1998). Fracture mechanics approach to penetration of surface crevasses on glaciers. *Cold Regions Science and Technology*, *27*(1), 31–47.
Vaughan, D. G. (1995). Tidal flexure at ice shelf margins. *Journal of Geophysical Research*, *100*(B4), 6213–6224.
Walker, C., Bassis, J., Fricker, H., & Czerwinski, R. (2013). Structural and environmental controls on Antarctic ice shelf rift propagation inferred from satellite monitoring. *Journal of Geophysical Research: Earth Surface*, *118*, 2354–2364. https://doi.org/10.1002/2013JF002742
Walker, C. C., Bassis, J. N., Fricker, H. A., & Czerwinski, R. J. (2015). Observations of interannual and spatial variability in rift propagation in the Amery Ice Shelf, Antarctica, 2002–14. *Journal of Glaciology*, *61*(226), 243–252.
Wang, R., & Shen, H. H. (2010). Gravity waves propagating into an ice-covered ocean: A viscoelastic model. *Journal of Geophysical Research*, *115*, C06024. https://doi.org/10.1029/2009JC005591
Weertman, J. (1957). Deformation of floating ice shelves. *Journal of Glaciology*, *3*(21), 38–42.
Weertman, J. (1971). Theory of water-filled crevasses in glaciers applied to vertical magma transport beneath oceanic ridges. *Journal of Geophysical Research*, *76*(5), 1171–1183.
Weertman, J. (1973). Can a water-filled crevasse reach the bottom surface of a glacier, *IASH Publications*, *95*, 139–145.
Weiss, J. (2004). Subcritical crack propagation as a mechanism of crevasse formation and iceberg calving. *Journal of Glaciology*, *50*(168), 109–115.
Williams, R., & Robinson, E. (1981). Flexural waves in the Ross Ice Shelf. *Journal of Geophysical Research*, *86*(C7), 6643–6648.
Yu, H., Rignot, E., Morlighem, M., & Seroussi, H. (2017). Iceberg calving of Thwaites Glacier, West Antarctica: Full-Stokes modeling combined with linear elastic fracture mechanics. *The Cryosphere*, *11*(3), 1283–1296. https://doi.org/10.5194/tc-11-1283-2017